applied sciences

MDPI

Article

Estimation of the Ultimate Strength of FRP Strips-to-Masonry Substrates Bond

Reza Kamgar [1], Houman Ebrahimpour Komleh [2], Anna Jakubczyk-Gałczyńska [3] and Robert Jankowski [3,*]

[1] Department of Civil Engineering, Faculty of Engineering, Shahrekord University, Shahrekord 88186-34141, Iran
[2] Department of Civil Engineering, Faculty of Engineering, Shahid Bahonar University of Kerman, Kerman 76169-13439, Iran
[3] Faculty of Civil and Environmental Engineering, Gdansk University of Technology, 80-233 Gdansk, Poland
* Correspondence: jankowr@pg.edu.pl

Abstract: Fiber-Reinforced Polymers (FRP) were developed as a new method over the past decades due to their many beneficial mechanical properties, and they are commonly applied to strengthen masonry structures. In this paper, the Artificial Neural Network (ANN), K-fold Cross-Validation (KFCV) technique, Multivariate Adaptive Regression Spline (MARS) method, and M5 Model Tree (M5MT) method were utilized to predict the ultimate strength of FRP strips applied on masonry substrates. The results obtained via ANN, KFCV, MARS, and M5MT were compared with the existing models. The results clearly indicate that the considered approaches have better efficiency and higher precision compared to the models available in the literature. The correlation coefficient values for the considered models (i.e., ANN, KFCV, MARS, and M5MT) are promising results, with up to 99% reliability.

Keywords: Fiber-Reinforced Polymers; Artificial Neural Network; K-fold Cross-Validation; Multivariate Adaptive Regression Spline; M5 Model Tree

Citation: Kamgar, R.; Komleh, H.E.; Jakubczyk-Gałczyńska, A.; Jankowski, R. Estimation of the Ultimate Strength of FRP Strips-to-Masonry Substrates Bond. *Appl. Sci.* **2023**, *13*, 6955. https://doi.org/10.3390/app13126955

Academic Editors: Raffaele Pucinotti and Young Hoon Kim

Received: 3 March 2023
Revised: 5 June 2023
Accepted: 5 June 2023
Published: 8 June 2023

1. Introduction

Fiber-Reinforced Polymers (FRPs) are commonly used for strengthening concrete structures (see [1,2]). These materials are also applied to strengthen masonry and steel structures due to the various benefits of FRP (e.g., outstanding corrosion resistance, high strength-to-weight ratio, and ability to change behavior under elevated temperatures [3–12]).

It is obvious that historical buildings should be preserved and inherited for future generations. Therefore, the utilization of innovative materials and technologies is important and justified for these objects, especially those at seismic risk. FRP is one of the most common new materials used to improve the seismic performance of historical buildings [13], mainly due to the damping properties of the polymers [14–16]. In connection with this fact, many studies were conducted on the behavior of FRP sheets in different configurations in strengthening the structural members, especially in masonry buildings. For example, in [17], the anchorage performance of FRP in solid clay bricks was studied. The bond–slip relationship of FRP sheets to the brick elements was also investigated in [18], being subjected to dynamic loading.

Recent investigations also showed that FRP sheets can increase the in- and out-of-plane lateral resistance of masonry structures [19]. A few research results can be mentioned at this point. The FRP sheets were used to improve the shear and flexural behavior of masonry wallets [20]. The glass fiber-reinforced polymer (GFRP) sheets were used to improve the out-of-plane resistance of masonry walls [21]. There are also results related to the strengthening of masonry elements using FRP bars and sheets [22,23]. It was also shown that the FRP sheets enhance the out-of-plane load capacity of the strengthened structures [24,25]. In the meantime, some experimental studies focused on the masonry structures strengthened with FRP sheets subjected to monotonic and cyclic loading [26,27].

Moreover, researchers investigated the effect of different bonded lengths of FRP sheets on the calcarenite stone behavior [28]. In other studies [29–31], experimental tests were applied to present mathematically based models to define the behavior of strengthened materials with FRP sheets. Grande et al., considered the micro-mechanical and macroscopic models used to study the behavior of FRP-reinforced and unreinforced masonry structures. The proposed models utilized different yielding criteria and constitutive laws [29]. There are arch and curved masonry structures that need to be retrofitted using FRP strips. Yuan and Milani [32] utilized the FRP sheets to enhance the capability to transform the tensile stress between the arch masonry and FRP sheets. Finally, they proposed a closed-form model. Castellano et al. [33] proposed a numerical model to study the responses of curved masonry structures retrofitted using fiber-reinforced cementitious matrix. They concluded that the numerical model needs fewer mechanical properties and computational costs and has high accuracy [33]. Jing et al. [34] performed experimental tests that retrofitted masonry walls using carbon fiber-reinforced polymer embedded in the mortar joint. They concluded that the combined structure failed on the shear mode via a diagonal configuration [34].

Recently, a model has been proposed in [35] which may reasonably predict the joint sliding for the masonry buildings retrofitted using pultruded FRP. Cecchi et al. [35] found that FRP-transfer length significantly affects the maximum monotonic load capacity of strengthened masonry panels. They also showed that the optimal transfer length depends on the average tensile strength of support and FRP stiffness per width. In [36], it was shown that a similar pattern for the transfer mechanism occurs in the masonry members strengthened with FRP sheets compared to the concrete members. They also proved that the strain path along the FRP sheets obeys different laws based on the magnitude of the applied load. A new method was also proposed to solve or delay the inopportune debonding of FRP sheets from the masonry wall surface [37]. Emami et al. [37] applied different strengthening methods (i.e., nailing, surface preparation, grooving, plaster, and boring) to mount the CFRP and GFRP sheets to the wall surfaces, and showed a 110% increase in the ductility index of reinforced walls. Furthermore, the ductility of reinforced walls improved by 26% and 53% for the surface preparation and boring methods, in combination with the nailing method, respectively [37]. In addition, the results showed that the ductility of the reinforced wall increased by 30% when the groove dimensions were 4 mm and 7 mm in width and depth, respectively. Finally, the cement plaster had no tangible effects in terms of improving the ductility of the wall. Mazzuca et al. [10] examined the effect of elevated temperature on the mechanical properties of glass fiber-reinforced polymer. They showed a mass reduction in the shear modulus and compressive strength due to the impact of the elevated temperature (i.e., 200 °C). In addition, Carvelli et al. [11] studied the effect of localized elevated temperatures on the static behavior of concrete members retrofitted with glass fiber-reinforced polymer. They showed that the value of reduction in the loading capacity depends on reinforcing geometry, especially in the overlapping area.

The use of novel, innovative technologies and materials, e.g., FRP, involves the obligation to perform a lot of research and testing to confirm its effectiveness. It is also possible to use soft techniques in addition to research and tests. Nowadays, soft computing techniques were widely accepted to predict the behavior of engineering problems [38,39]. For a unique issue, the accuracy of the results depends on the method selected for solving the problem. There are different well-known soft computing techniques. For example, [38] utilized the neuro-fuzzy and neural network techniques to forecast debonding behavior of FRP sheets in masonry elements. They concluded that an optimal adaptive neuro-fuzzy inference system predicted the bond strength of FRP-to-masonry elements by 39% and 23% in the form of root mean square errors and mean absolute errors, respectively, compared to the optimal multiple non-linear regression models. The genetic programming (GP) method was applied to assess the bond strength of the FRP-to-concrete composite joint [40]. Finally, an empirical formula based on the GP model was proposed by Abdellahi et al. [40], which showed an appropriate agreement with the experimental results.

Researchers utilized different soft computing techniques to discover the existing behavior between the parameters in an engineering problem. For example, the parallel hyper-cubic gene expression programming method was used to measure slump flow [41]. Soft computing methods (i.e., stepwise regression, neural network, neuro-fuzzy, and GP) were adopted to estimate the strength improvement of concrete cylinders confined using FRP [42]. The neuro-fuzzy method, regression, and analytical models were also applied to offer a model for predicting the curvature and bending ductility factors for the high-performance concrete beams strengthened with CFRP sheets [43,44]. The gene expression programming technique was adopted in [45] to estimate the thermal behavior of evacuated tube solar collectors. The Multiple-Kernel Support Vector Regression algorithm was used to estimate the water quality parameter [46]. Other authors applied the Mars Model to predict the water quality index [47]. The analytical models only use a specific dataset; therefore, they can predict engineering problems with lower accuracy [48]. Kumar et al. [48] proposed new models to predict the fiber-reinforced cementitious matrix to concrete bond utilizing robust soft models (i.e., curve-fitting, Gaussian Process Regression, and the Adaptive Neuro-Fuzzy Inference System). They also performed a sensitivity analysis to find the critical parameter in predicting the fiber-reinforced cementitious matrix to concrete bond [48].

Based on the published scientific background, it can be concluded that soft techniques may be a good solution to predict the existing relationship between the parameters in an engineering problem. Therefore, this paper utilizes four robust techniques (i.e., ANN, KFCV, Mars, and M5 model tree techniques) to forecast the ultimate strength of FRP-to-masonry bond. In fact, this paper uses four robust techniques to develop new formulae with higher precision than the existing examples. In this regard, we tried to decrease the computational cost by introducing new parameters to reduce the number of input parameters. It should be noted that soft computing techniques can provide a simple and accurate preliminary design process for engineers that is acceptable based on ACI 440-7R-10 [49] and CNR-DT 200 [50] codes. These results can also be used in the design process, although the design reliability coefficients should be calibrated in separate studies.

2. Research Objectives

In the scientific community, there are models that can predict the ultimate strength of FRP-to-masonry bonded joints. An overview of these models (see Section 2.1) shows that an even better model with more efficiency can be present, since the existing models have two defects: some of them have no high precision (see Section 4 and Table 1, e.g., Khalifa model, De Lorenzis model, Maeda et al., model), and the others have more parameters (some of which require initial computing, after which the ultimate strength of a FRP strips-to-masonry substrates bond can be computed (see Table 1), e.g., Neubauer and Rostasy model, Iso model, Willis et al., model, etc.). These models will lead to some formula being hard to integrate with them. Therefore, the main objective of the paper is to present new formulas to compute the ultimate bond strength of FRP and masonry joints with high precision to overcome those above-mentioned challenges. In the technical literature, the pull-out test presents the bond strength of FRP-to-masonry joint regarding debonding failure mechanisms as the most widespread bond test setup. Although there are different experimental methods for assessing bond capacity, no standard procedures have yet been presented. Based on [51], the pull-out test in a single shear setup is considered the most reliable setup to study FRP-to-masonry joint bond members. Therefore, the existing single shear test (pull-out) results are selected to create the soft computing models and evaluate the bond strength.

2.1. Overview of Existing Formulas

In order to present the existing formulas for assessing the ultimate bond strength (P_{max}) for members with materials that failed in a brittle manner and were strengthened with FRP sheets, the overview was executed, and Table 1 is presented. Some of the existing formulae (i.e., Kashyap et al. [7], Camli and Binici [3], and Willis et al. [52]) were valid for the masonry

materials. The others were valid for the concrete substrate, which had a similarly brittle manner; therefore, they could be compared with the considered dataset. There were some differences between masonry and concrete substrates. Nonetheless, all of these formulas were studied in previous research to show the viability of the proposed approach [7,19]. The origin of some differences could be found in compressive strength levels, microscopic behaviors, and the brittle failure surface by considering internal reinforcement (Calmi and Binici [3]). It was noted that by considering these references, the formulas proposed for the concrete substrates were utilized by researchers for the masonry substrates [7].

Most of these formulas were obtained via empirical methods that lead to lower accuracy (see Section 4). Therefore, soft computing techniques were used to obtain new formulas with higher accuracy.

An investigation of the available formulas proved that all of the existing formulas were functions of the thickness of the FRP strip (t_p), the width of the FRP strip (b_p), the elasticity modulus of the FRP strip (E_p), the width of the masonry block (b_m), the bonded length (l_b), and the tensile strength of the masonry block (f_{ut}), respectively. Figure 1 displays a schematic of a masonry block strengthened with a FRP strip in the form of a pull-out test [19]. In [3,7], some configurations of the test setup, measurement protocols, etc., were experimentally illustrated in more detail. Almost all of the pull-out test in a direct shear test manner was used to study the bond response of FRP to brittle substrates (e.g., masonry blocks) [53]. During test procedures, strains and surface displacements were obtained from optical techniques, such as digital image correlation (DIC) or electromechanical gages, in the form of strain gages and Linear Variable Deformational Transformers (LVDTs). In the test setup, the FRP sheets were mounted on the masonry blocks using epoxy, and the tensile loading was applied to the FRP sheet to pull it out. Consequently, by considering supports applied perpendicular to the direction along the loaded FRP, the stability of the setup was satisfied.

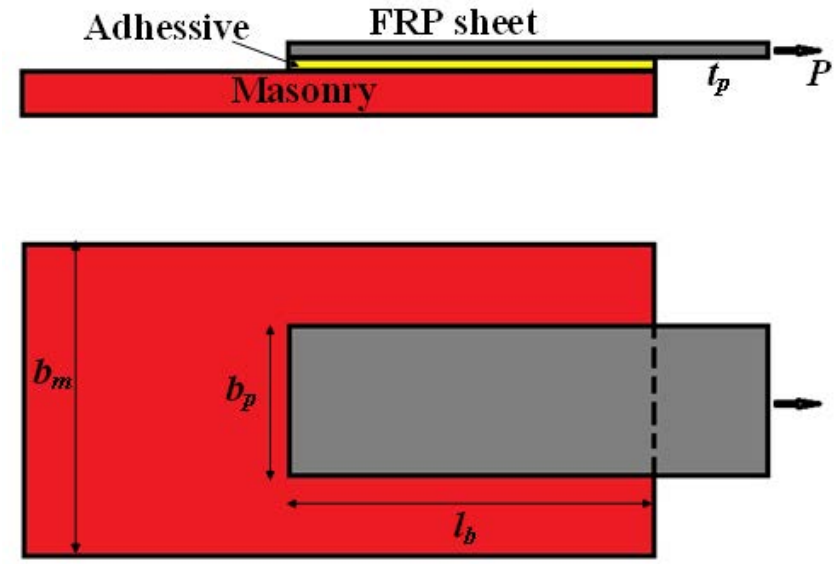

Figure 1. A scheme of a masonry block strengthened with a FRP strip.

Table 1. Existing formula for forecasting ultimate bond strength of masonry members strengthened using FRP sheets (some of formulas presented here are extracted directly from [19]).

Model's Name	References	Existing Equations
Khalifa	[54]	$P_{\max} = 110.2 \times 10^{-6} \times \left(\frac{f'_{cm}}{42}\right)^{\left(\frac{2}{3}\right)} \times E_p \times t_p \times l_e \times b_p$ $l_e = e^{6.134-0.58\times\ln(E_p\times t_p)}$ unit of E_p is GPa

Table 1. *Cont.*

Model's Name	References	Existing Equations
De Lorenzis	[55]	$P_{\max} = b_p \times \sqrt{2 \times E_p \times t_p \times G_c}$ $G_c = 1.43\ (\frac{N.mm}{mm^2})$
Tanaka	[5]	$P_{\max} = l_b b_p (6.13 - \ln l_b)$
Maeda et al.	[6]	$P_{\max} = 110.2 \times 10^{-6} \times E_p \times t_p \times l_e \times b_p$ $l_e = e^{6.134 - 0.58 \times \ln(E_p \times t_p)}$ unit of E_p is GPa
Dai	[56]	$P_{\max} = (b_p + 7.4) \times \sqrt{2 \times E_p \times t_p \times G_c}$ $G_c = 0.514 \times f'^{0.236}_{cm}$
Accardi	[28]	$P_{\max} = b_p \times \sqrt{12 \times E_p \times t_p \times \sqrt{f'_{cm}}}$
Sato et al.	[57,58]	$P_{\max} = 2.68 \times 10^{-5} \times (f'_{cm})^{0.2} \times E_p \times t_p \times l_e \times (b_p + 7.4)$ $l_e = 1.89 \times (E_p \times t_p)^{0.4}$ if $l_b \geq l_e$
Iso	[57]	$P_{\max} = 0.93 \times (f'_{cm})^{0.44} \times b_p \times l_e$ $l_e = 0.125 \times (E_p \times t_p)^{0.57}$ if $l_b \geq l_e$
Yang et al.	[57,59]	$P_{\max} = (0.5 + 0.08 \times \sqrt{\frac{0.01 \times E_p \times t_p}{f_{ut}}}) \times \frac{L_e \times b_p \times f_{ut}}{2}$ $l_e = 100\ (\text{mm})$
Willis et al.	[52]	$P_{\max} = 1.45 \times \phi_f^{0.263} \times f_{ut}^{0.6} \times \sqrt{l_{per} \times E_p \times t_p \times l_b}$ $\phi_f = \frac{1}{2 + b_p}$ for EB case $l_{per} = 2 + b_p$
Kashyap et al.	[5]	$P_{\max} = 13.69 \times \phi_f^{0.84} \times f_{ut}^{0.9} \times \sqrt{l_{per} \times E_p \times t_p \times l_b}$ $\phi_f = \frac{1}{2 + b_p}$ for EB case $l_{per} = 2 + b_p$
Neubauer and Rostàsy	[60,61]	$P_{\max} = \begin{cases} 0.64 \times k_p \times b_p \times \sqrt{f_{ut} \times E_p \times t_p} & \text{if } l_b \geq l_e \\ 0.64 \times k_p \times b_p \times \sqrt{f_{ut} \times E_p \times t_p} \times \alpha & \text{if } l_b < l_e \end{cases}$ $l_e = \sqrt{\frac{E_p \times t_p}{2 \times f_{ut}}}$ $\alpha = (\frac{l_b}{l_e})(2 - \frac{l_b}{l_e})$ $k_p = \sqrt{1.125 \times \frac{2 - \frac{b_p}{b_m}}{1 + \frac{b_p}{400}}}$
Van Gemert	[60,62]	$P_{\max} = 0.5 \times l_b \times b_p \times f_{ut}$
Mansouri et al.	[19]	$P_{\max} = [f_{ut}^{1.5} \times L_b - L_b \times t_p \times c_1] + [f_{ut}^3 \times b_m - b_p^2 \times t_p]$ $+ [L_b^{1.5} + c_2 + \frac{t_p}{c_0} \times (L_b + E_p)]$ $c_1 = 9.941346$ $c_2 = 9.58728$ $c_0 = 9.351684$
Camli and Binici	[3]	$P_{\max} = \sqrt{\tau_f \times \delta_u} \times \sqrt{E_p \times t_p} \times b_p \times \tanh\left(\frac{\theta \times l_p}{l_e}\right)$ $\theta = \sqrt{\frac{\tau_f}{\delta_u \times \sqrt{f'_{cm}}}}$ $l_e = \sqrt{\frac{E_p \times t_p}{\sqrt{f'_{cm}}}}$ $\tau_f = \omega \times f'^{0.19}_{cm}$ ω is a coefficient that depends on the substrate material type (see Ref. [3]) $\delta_u = f'^{\alpha}_{cm} \left(\frac{l_p}{l_e}\right)^{\beta} \left(\frac{b_p}{b_m}\right)^{\gamma}$ α, β and γ are exponents that can be determined by nonlinear regression analysis based on Ref. [3]

Table 1. *Cont.*

Model's Name	References	Existing Equations
Chen and Teng	[4]	$P_{\max} = 0.427 \times \beta_p \times \beta_L \times \sqrt{f'_{cm}} \times b_p \times l_e$ $l_e = \sqrt{\frac{E_p \times t_p}{\sqrt{f'_{cm}}}} \quad \beta_p = \sqrt{\frac{2-\frac{b_p}{b_m}}{1+\frac{b_p}{b_m}}}$ $\beta_L = \begin{cases} 1 \text{ if } l_b \geq l_e \\ \sin\frac{\pi \times l_b}{2 \times l_e} \text{ if } l_b < l_e \end{cases}$
Wu and Jiang	[63]	$P_{\max} = k_L \times E_p \times t_p \times b_p \times \frac{\alpha}{\beta}$ $k_L = \frac{\eta \times \sqrt{1-\eta^2} \times \sinh(\sqrt{1-\eta^2} \times \frac{l}{\beta})}{1+\eta \times \cos h(\sqrt{1-\eta^2} \times \frac{l}{\beta})}$ $l_e = 2 \times Ln(\frac{1+\delta}{1-\delta}) \times \beta \qquad \frac{\alpha}{d} = 0.094 \times (\frac{f_{cm}}{E_d})^{0.026}$ $k_w = \lambda + (1-\lambda) \times \frac{b_p}{b_m} \quad \lambda = 1 + 0.222 \times (\frac{f_{cm}}{E_f})^{0.304}$ $\frac{\beta}{d} = \frac{0.134 \times (\frac{E_f \times t_f}{E_d \times d})^{0.5}}{k_w \times (\frac{f_{cm}}{E_d})^{0.082}}$ $\eta = -3.61e^{-0.4454\frac{l}{\beta}} + 4.11e^{-0.3835\frac{l}{\beta}}$

In Table 1, f'_{cm} and f_{ut} are the compressive and tensile strength of masonry in the MPa unit and defined as follows:

$$f_{ut} = 0.53 \times \sqrt{f'_{cm}} \tag{1}$$

It should be noted that in Table 1, Tanaka and Maeda models were reported from [4]. Moreover, Sato, Iso, and Yang models were extracted from [57]. Finally, Neubauer and Van-Gemert models were presented here from [60]. It should be noted that equations available in the literature (see Table 1) referred to specific geometry and materials in most cases.

3. Prediction with New Models

A set of experimental data was gathered from the literature to present a new model for determining the P_{max} value [3,8,9,52,64–69]. The number of collected literature-based data values was 134 (see Appendix A), which were extracted from [5,19]. A set of re-grouping parameters (a, b, c, d, and F) were introduced from the collected data, and these parameters were classified into the input/output parameters (see Table 2). According to Table 1, it can be understood that some existing models needed more input parameters to compute the P_{max} value with a better prediction (i.e., in some existing models, such as that of Tanaka [4], only two parameters were needed to define the model). Although their formula was easy to work, they haf a large error [19]. In this regard, based on [19], the existing models had little accuracy based on R^2 and root mean-squared error (RMSE) criteria. Finally, for simplicity, only [19] was considered here as a new work with better accuracy to show the ability of the proposed formulas. Therefore, basic geometric and engineering parameters were defined here, where a, b, c, and d show the axial stiffness of the FRP per width, the width ratio for FRP with respect to masonry block, the bonded length of FRP, and the ultimate tensile strength of the masonry block, respectively. In fact, these considered parameters were defined here based on Table 1 through means of practical engineering issues and to decrease the number of input parameters previously used in the existing formulas (see Table 1). More discussions are presented in Section 4.

Table 3 presents these data's statistical properties (i.e., maximum, minimum, coefficient of variation, mean, and standard deviation).

The following sections present four robust techniques (i.e., ANN, KFCV, Mars, and M5 model tree techniques). They were applied to predict the ultimate strength of the FRP-to-masonry bond. These techniques were selected as they are the most popular and well-known techniques used in input–output fitting problems.

Table 2. Newly proposed parameters.

Type	Parameters
Input	$a = t_p \times E_p$(kN/mm)
	$b = b_p/b_m$ (mm/mm)
	$c = l_b$(mm)
	$d = f_{ut}$(MPa)
Output	$F = P_{\max}/b_p$ (kN/mm)

Table 3. Statistical properties of experimental data.

Quantity	t_p(mm)	E_p(kN/mm^2)	b_p(mm)	l_b(mm)	b_m(mm)	f_{ut}(MPa)	$P_{\max}$(kN)
Mean	0.877	120.719	32.781	170.440	347.127	2.232	15.630
Minimum	0.12	22.3	6.35	50	200	0.780739	2.13
Maximum	6.35	230	50	420	740	3.57	84.5
Standard deviation	1.058	83.490	13.842	105.624	197.375	0.965	20.013
Coefficient of variation	1.202	0.689	0.421	0.617	0.566	0.431	1.276

3.1. The ANN Model

Artificial Neural Networks are a good predictive tool used for engineering problems [70,71]. Their operation is based on the principle of the prosperity of the nervous system. The data are divided into three sets: training, validation, and testing. ANN is composed of layers, neurons, and weights. The main task of the network is to find a pattern of connections and relationships between inputs and outputs [71]. There are many types of networks [71,72]. A feed-forward neural network involves three types of layers: input, hidden, and output layers (see Figure 2).

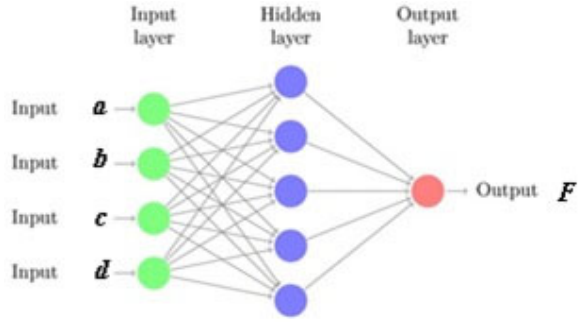

Figure 2. A schematic model of a three-layer neural network: input signals (*a*–*d*) and output signal *F*.

Here, the log-sigmoid transfer function was utilized in the ANN model. Furthermore, one hidden layer was used in this model. At first, all collected data were normalized using the below equation [2]. Next, the normalized data were accepted for three stages, including training, validating, and testing. Since ANN uses the log-sigmoid transfer function to avoid the saturation problem, collapse on the border values, and, consequently, a low training rate, the mapping function converted the real input values to corresponding values in the range of 0.1–0.9. It should be noted that this range w usual in the pre-processing of datasets in engineering applications [71].

$$\begin{aligned} g_{scaled} &= (0.9 - 0.1)\left(\frac{g - g_{\min}}{g_{\max} - g_{\min}}\right) + 0.1 \\ 0.1 &\le g_{scaled} \le 0.9 \end{aligned} \tag{2}$$

where g, $g_{\min}$, $g_{\max}$, and g_{scaled} are the selected data, the minimum value of data, the maximum value of data, and the scaled value for the data, respectively. This study adopted the Levenberg–Marquardt algorithm for training, validating, and testing datasets. Firstly, various sets were examined to find the optimum distribution of the dataset (training, validating, and testing sets are 70%, 15%, and 15% of all datasets, respectively). A 4:*n*:1 network was chosen. This network had four inputs, *n* hidden neurons, and one output (see Figure 2). A criterion should be supposed to check and stop the training step of the network. The mean-squared error (MSE) was selected as the criterion. Moreover, a better performance was expected for the desired network when the minimum value of MSE was computed. This study measures the correlation between the targets and outputs using the regression values (R-values). The criteria mentioned above were utilized to identify a network with a better performance. The regression values of the different networks for various numbers of neurons in the hidden layers are presented in Figure 3. The maximum error values for each network are depicted in Figure 4. Figures 3 and 4 represent the finding that a network with ten hidden neurons performs most effectively.

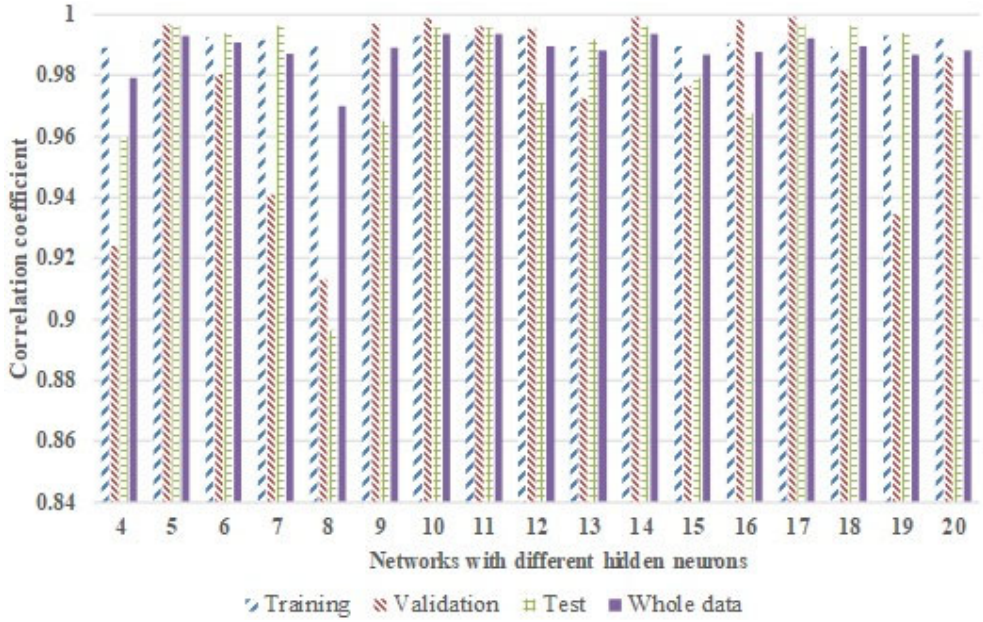

Figure 3. Performance of correlation coefficient for various ANN models (4:*n*:1).

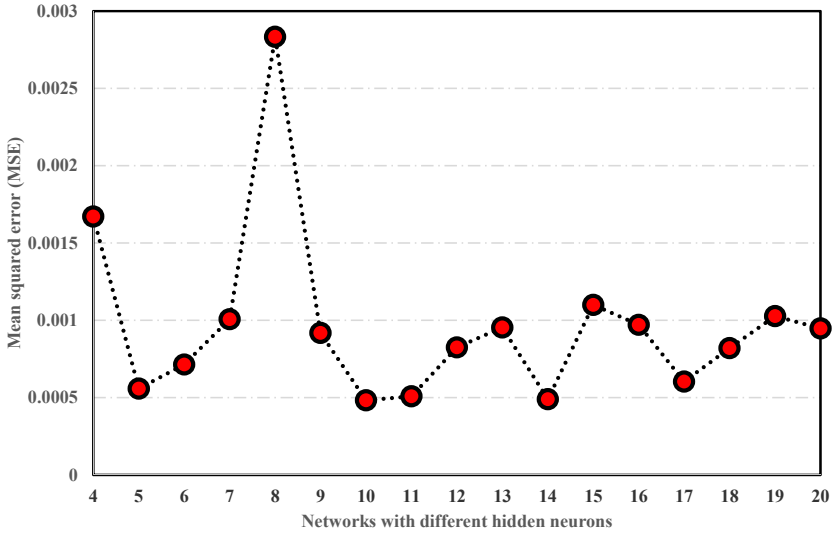

Figure 4. Values of mean-squared errors for various numbers in hidden neurons.

Figures 5–7 show the results for the training of the selected network (*4-10-1*). Moreover, Figure 5 exhibits the excellent performance of the selected network. Furthermore, in Figure 7, the training state parameters, such as performance gradient, mu (i.e., the momentum constant), and validation failing (i.e., val fail) epoch, are illustrated based on the Levenberg–Marquardt algorithm [71].

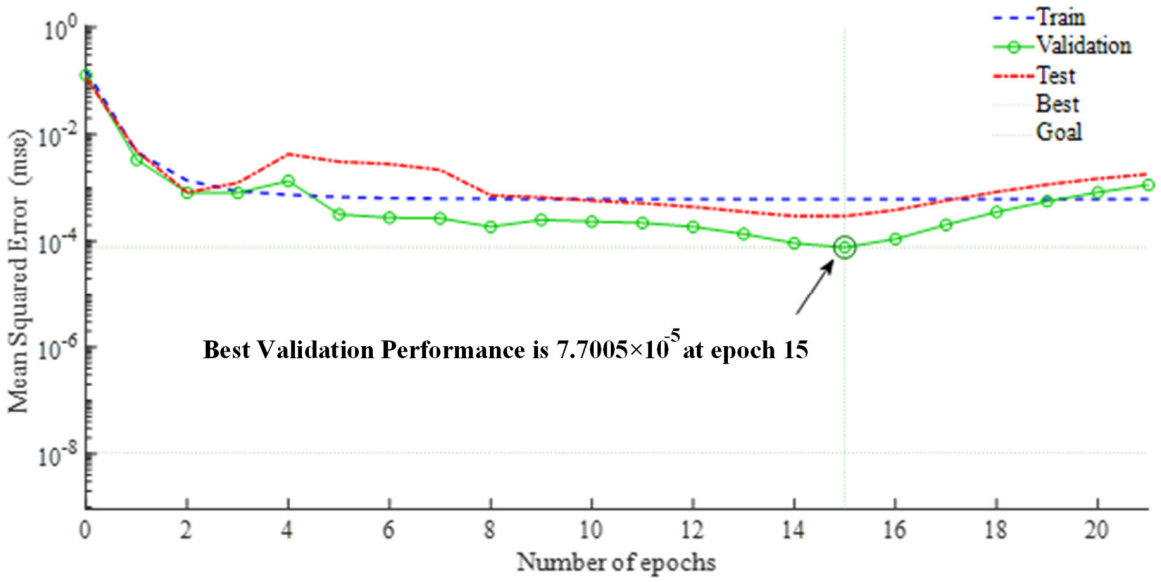

Figure 5. Values of mean-squared errors for various numbers of epochs.

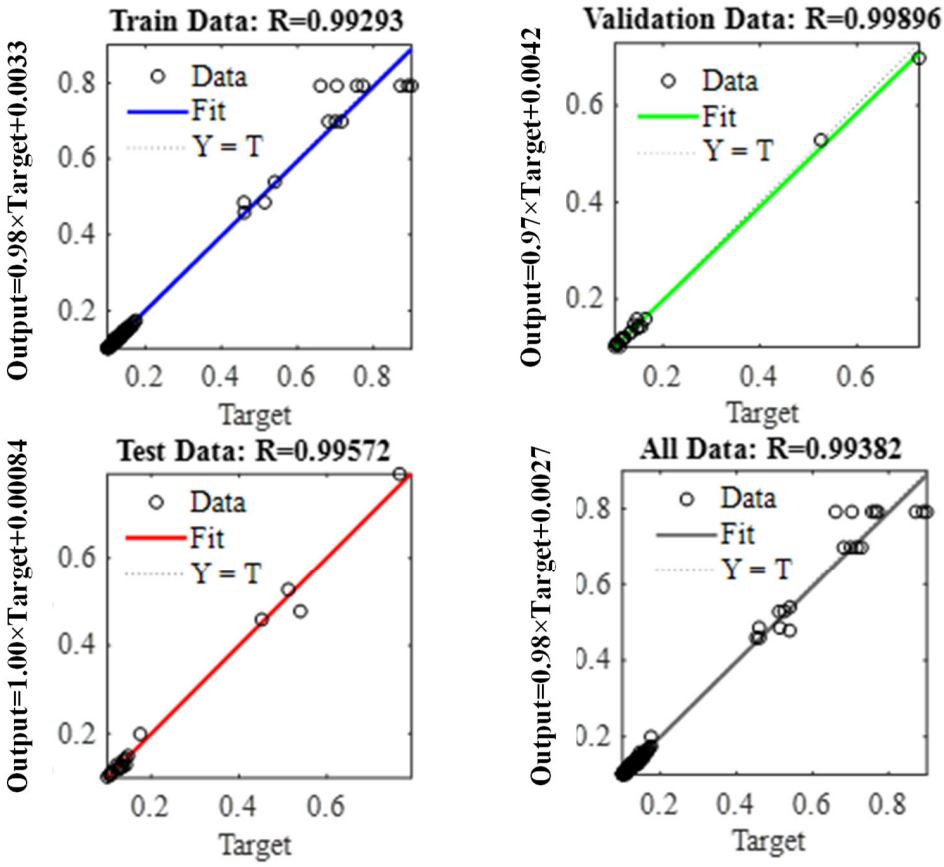

Figure 6. Regression of training, testing, and validation of datasets simulated via ANN for *4-10-1*.

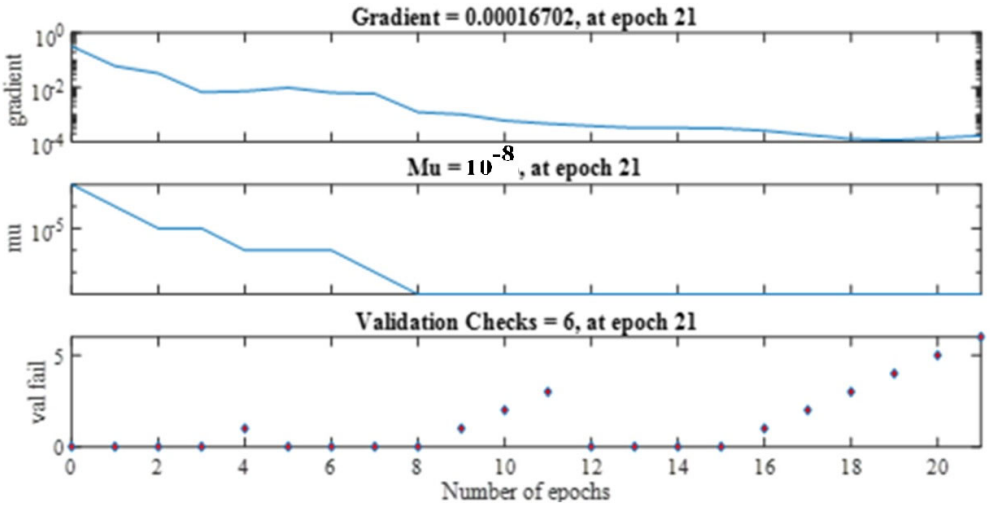

Figure 7. Training state of ANN for *4-10-1*.

3.2. The ANN Model with K-Fold Cross-Validation (KFCV)

This section used the Feed-Forward Back Propagation Neural Network (FFBPNN) to forecast the ultimate strength of FRP strips applied on masonry elements [2,72,73]. Firstly, all data should be arranged randomly into *K* folds. The *K-1* folds were utilized in the training step from the data, and the last fold was maintained for the neural network test. Different values for the *K* parameter were examined (e.g., *K* = 2, 3, 4, 5) to obtain the best values. Finally, the performance of each neural network was analyzed using the percentage of corrected prediction for *K* folds. Finally, the correct classification factor (CCF) and the percentage of area under the CCF (AUCCF) for different ANN structures were utilized to determine the optimal epoch. For this problem, a neural network with three layers was chosen.

Furthermore, the AUCCF was measured until the optimal epoch was reached to optimize the neurons in the hidden layer. Therefore, the number of neurons changes from 2 to 13 in the hidden layers. Finally, by drawing the AUCCF, the structure with the best efficiency could be obtained. The AUCCF curve is displayed in Figure 8. It could be inferred that the *4-6-1* structure had the best performance (99.4%) in estimating the ultimate bond strength of FRP-to-masonry joints. Furthermore, Figure 9 confirmed that the optimal epoch for the *4-6-1* structure was 3.

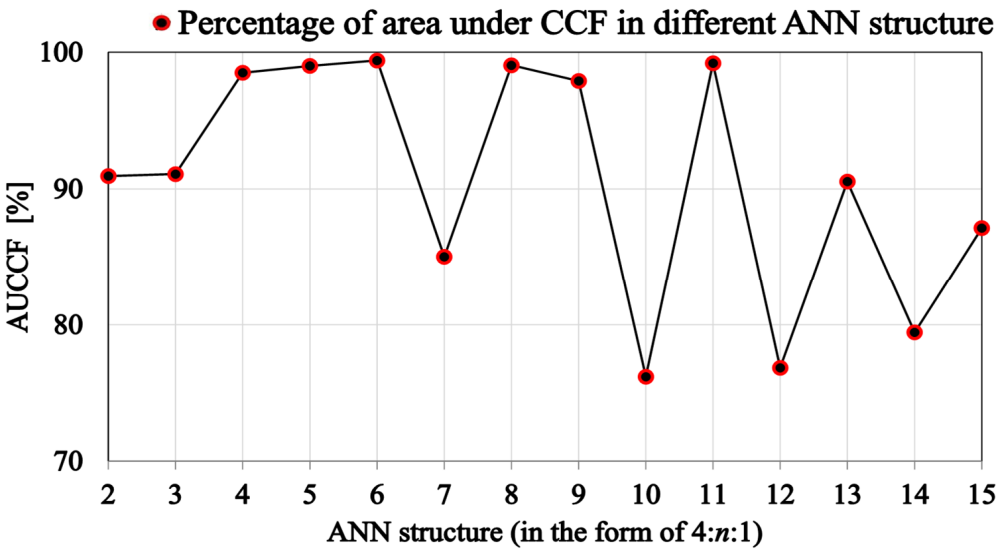

Figure 8. AUCCF curve for different neural networks.

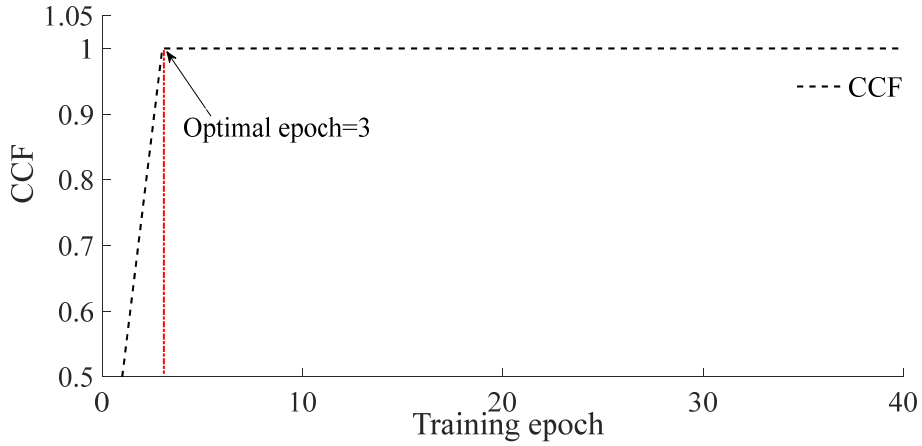

Figure 9. CCF curve for structure with pattern *4-6-1*.

The R^2 values for the optimized structure (*4-6-1*) are presented in Figure 10 to show the performance of the ANN neural network with six hidden layers. This figure reveals that the correlation coefficient of the ANN neural network with six hidden layers is 0.9871. It depicts the high efficiency of the ANN structure with pattern (*4-6-1*).

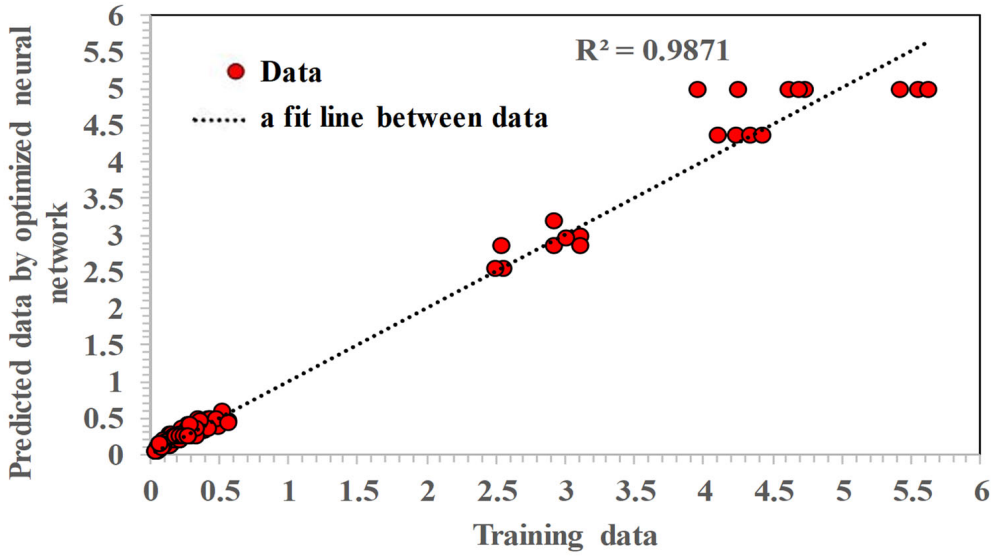

Figure 10. Correlation coefficient between training data and those estimated via optimized ANN structure.

It should be noted that different activation functions (i.e., the Tansig and Pureline functions, respectively) were considered here for hidden and output layers.

3.3. Multivariate Adaptive Regression Spline (MARS)

The MARS technique is an advanced regression model proposed in [74] using three main components: a linear regression model, non-parametric statistical analysis, and spline mathematical formulation [75]. In a general form, the MARS output can be defined based on a combination of the basic functions as follows:

$$\frac{P_{\max}}{b_p}(t_p \times E_p, b_p/b_m, l_b, f_{ut}) = \rho_0 + \sum_{i=1}^{s} \rho_i \times BF_i(t_p \times E_p, b_p/b_m, l_b, f_{ut}) \quad (3)$$

where ρ_0, ρ_i, BF_i, i, and s show the weighting coefficients, the basis function, the counter, and the number of basic functions, respectively. The Least Squares method computes the basic functions [75]. Moreover, the MARS technique uses the trial-and-adjustment

approach to provide a good relationship using the basic functions extracted based on Adaptive Piecewise Linear Regression (APLR) [74]. Generally, the MARS model can find an approximate function between the input variables and the output target. Therefore, this model will lead to a mathematical function. For the collected data [3,8,9,52,65–69], the following equation can be obtained using the MARS model:

$$\begin{aligned}\frac{P_{\max}}{b_p} &= 0.42521 + 0.015824 \times BF_1 - 0.11179 \times BF_2 \\ &\quad -194.2 \times BF_3 - 0.13415 \times BF_4 - 4.1329 \times 10^{-5} \times BF_5\end{aligned} \tag{4}$$

where

$$\begin{aligned}BF_1 &= \max\,(0,\ (t_p \times E_p) - 45.26) \\ BF_2 &= BF_1 \times \max\,(0,\ \tfrac{b_p}{b_m} - 0.089286) \\ BF_3 &= \max\,(0,\ f_{ut} - 3.55) \\ \mathrm{BF}_4 &= \max\,(0,\ 3.55 - f_{ut}) \\ \mathrm{BF}_5 &= \mathrm{BF}_1 \times \max\,(0,\ l_b - 328)\end{aligned} \tag{5}$$

3.4. M5 Model Tree (M5MT)

The model tree was introduced in 1992 in [76] and later modified in 1996 in [77]. The M5MT model can convert the non-linear behavior between the input and output variables into a linear form using multivariate linear regression. The M5MT model can change a complex problem to different linear models by dividing the search space into different sub-spaces. Next, a linear model is computed for each sub-space. Finally, combining linear models in each sub-space will lead to the overall output model. The implementation of the M5MT can be performed using Weka 3.9 software. Detailed information for this model can be studied from [76,77].

In this paper, the proposed equation for the studied problem using the M5MT model can be stated as follows:

$$\frac{P_{\max}}{b_p}(t_p \times E_p, b_p/b_m, l_b, f_{ut}) = C_0 + C_1 \times (t_p \times E_p) + C_2 \times \frac{b_p}{b_m} + C_3 \times l_b + C_4 \times f_{ut} \tag{6}$$

where C_i and i show the constant coefficients and the counter, respectively. For the collected data, the following equation can be obtained using the M5MT model:

$$\begin{aligned}\tfrac{P_{\max}}{b_p} &= 0.0015 \times\ (t_p \times E_p) - 1.4048 \times \tfrac{b_p}{b_m} + 0.0002 \times l_b + 0.1674 \times f_{ut} - 0.0283 \quad \text{for } l_b \le 225.5 \\ \tfrac{P_{\max}}{b_p} &= 0.0049 \times\ (t_p \times E_p) - 11.8451 \times \tfrac{b_p}{b_m} + 0.0006 \times l_b + 0.178 \times f_{ut} + 1.7105 \quad \text{for lb} > 225.5\end{aligned} \tag{7}$$

4. Results

Here, the efficiency and performance of the proposed model are investigated by comparing them with the existing models (see Table 1). Table 4 presents the values of R^2 and RMSE for various models.

Table 4. Values of R^2 and RMSE for different studied models.

Model's Name	References	R^2	*RMSE*
Khalifa	[54]	0.2833 *	1.103
De Lorenzis	[55]	0.2168 *	1.087
Tanaka	[5]	0.1088 *	1.319
Maeda et al.	[6]	0.1624 *	1.159
Dai	[56]	0.3837 *	0.953
Sato	[57,58]	0.6723 *	4.040
Iso	[57]	0.1179 *	1.714

Table 4. *Cont.*

Model's Name		References	R^2	*RMSE*
Yang et al.		[57,59]	0.2124 *	1.148
Willis et al.		[52]	0.4898 *	0.987
Kashyap et al.		[5]	0.8841 *	0.475
Neubauer and Rostàsy		[60,61]	0.3190 *	1.027
Van Gemert		[60,62]	0.1204 *	1.226
Mansouri et al.		[19]	0.9646	0.240
Camli and Binici		[3]	0.5425	1.869
Chen and Teng		[4]	0.478	0.96
Wu and Jiang		[63]	0.62	0.87
Present study	ANN	-	**0.9877**	**0.157**
	ANN-KFCV	-	**0.9871**	**0.159**
	MARS	-	**0.9839**	**0.176**
	M5MT	-	**0.9802**	**0.193**

* shows that these data are extracted from [19].

Based on Table 4, the R^2 values for the considered models (i.e., ANN, KFCV, MARS, and M5MT) are 0.9877, 0.9871, 0.9839, and 0.9802, respectively. The best value for this parameter is 0.9646 in the other existing models (i.e., model from [19]). Based on Table 4, the proposed models have fewer RMSE values than other empirical models. As described in Section 3, the mentioned configuration for the input/output parameters also utilized the well-known soft computing techniques, leading to high accuracy, low computational cost, and more feasibility for practical engineering applications.

Moreover, the RMSE (root mean-squared error), MAE (mean absolute error), MAPE (mean absolute percentage error), and correlation coefficient values for the considered models (i.e., KFCV, MARS, and M5MT) in comparison to the best existing model are proposed in Table 5. The best values for these parameters are shown in bold form. These results mean that the simulated results were consistent with the experimental results. It also shows that the considered models accurately forecast the ultimate strength of FRP strips applied on masonry substrates. Based on Table 4, the model suggested in [19] has more precision than the models available in the literature. Therefore, this model is chosen to compare with the considered models. Figure 11 shows the comparison between these models. From Figure 11 and Table 5, it can be inferred that the considered model (i.e., the KFCV technique) has more accuracy than the model presented in [19]. It should be noted that percentage values in Figure 11 show the underestimated and overestimated bounds as error zones.

Table 5. A comparison between the considered models and best existing model.

Method Error	ANN-KFCV	MARS	M5MT	Mansouri et al. [19]
MAPE (%)	**19.08**	21.02	27.10	19.31
RMSE	**0.159**	0.176	0.193	0.24
AAE	**0.0778**	0.0917	0.1036	0.1144
Correlation coefficient	**0.9935**	0.9919	0.9900	0.9853

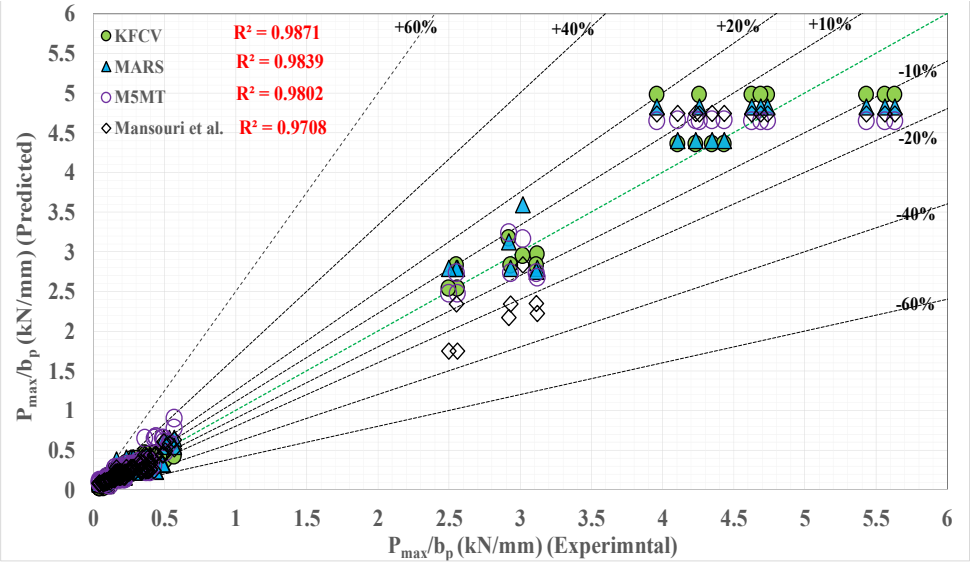

Figure 11. A comparison between considered model (i.e., KFCV, MARS, and M5MT models) and best existing model (i.e., model presented in [19]).

5. Summary

This paper presents the ANN, ANN-KFCV, MARS, and M5MT techniques to estimate the ultimate strength of FRP strips applied on masonry substrates. Firstly, knowledge and possible solutions were reviewed. In the next stage, a set of experimental data (134 cases) was gathered and normalized. Finally, ANN, KFCV, MARS, and M5MT techniques were applied to offer new models predicting the ultimate bond strength of FRP strips to masonry joints. The R^2 values in the ANN method amount to 0.99293, 0.99896, 0.99572, and 0.99382 for training, validation, testing, and all data, respectively. Furthermore, this value is 0.9935, 0.9919, and 0.9901 for the KFCV, MARS, and M5MT methods. The results prove that the established techniques have an excellent coincident with the experimental values. This finding confirms the accuracy of the proposed formulas in forecasting the ultimate strength of FRP strips applied to masonry elements. In this regard, we tried to decrease the computational cost by introducing new parameters to reduce the number of input parameters. It should be noted that the proposed formulas are valid for externally bonded FRP-to-masonry members. The results show that the presented formulas are more precise than the existing formulas.

Author Contributions: Conceptualization, R.K. and H.E.K.; methodology, R.K., H.E.K., A.J.-G. and R.J.; software, R.K. and H.E.K.; validation, R.K., H.E.K., A.J.-G. and R.J.; formal analysis, R.K. and H.E.K.; investigation, R.K. and H.E.K.; writing—original draft preparation, R.K. and H.E.K.; writing—review and editing, A.J.-G. and R.J. All authors have read and agreed to the published version of the manuscript.

Funding: This research received no funding.

Institutional Review Board Statement: Not applicable.

Informed Consent Statement: Not applicable.

Data Availability Statement: The datasets generated and analyzed during the current study are available on request.

Conflicts of Interest: The authors declare no conflict of interest.

Appendix A

The database categorized based on the literature review of existing experimental bond tests for FRP-to-masonry joints is presented as follows:

Table A1. The properties of the dataset based on experimental samples collected from existing literature.

No.	tp (mm)	Ep (GPa)	bp (mm)	lb (mm)	bm (mm)	fut (MPa)	Pmax (kN)	Ref. No. (Year)
1	6.35	40.8	6.35	254	230	1.93	19.17	[64] (2003)
2	6.35	40.8	6.35	381	230	1.93	18.55	
3	1	22.3	25	50	400	2.05	4.88	[65] (2005)
4	1	22.3	25	50	400	2.05	5.63	
5	1	22.3	25	50	400	2.05	4.25	
6	1	22.3	25	50	400	2.05	3.75	
7	1	22.3	25	50	400	2.05	5.13	
8	1	22.3	25	75	400	2.05	5.81	
9	1	22.3	25	75	400	2.05	5.44	
10	1	22.3	25	75	400	2.05	6.38	
11	1	22.3	25	75	400	2.05	3.94	
12	1	22.3	25	75	400	2.05	7.13	
13	1	22.3	25	100	400	2.05	4.75	[65] (2005)
14	1	22.3	25	100	400	2.05	5	
15	1	22.3	25	100	400	2.05	6.5	
16	1	22.3	25	100	400	2.05	7.25	
17	1	22.3	25	100	400	2.05	7.25	
18	1	22.3	25	100	400	2.05	8.5	
19	1	22.3	25	50	200	2.73	9.25	
20	1	22.3	25	50	200	2.73	7.38	
21	1	22.3	25	50	200	2.73	8.63	
22	1	22.3	25	50	200	2.73	6.88	
23	1	22.3	25	75	200	2.73	10.69	
24	1	22.3	25	75	200	2.73	8.44	
25	1	22.3	25	75	200	2.73	9.38	
26	1	22.3	25	75	200	2.73	9.56	
27	1	22.3	25	75	200	2.73	8.25	
28	1	22.3	25	100	200	2.73	8.5	
29	1	22.3	25	100	200	2.73	10	
30	1	22.3	25	100	200	2.73	10	
31	1	22.3	25	100	200	2.73	9	
32	1	22.3	25	100	200	2.73	10	
33	1	22.3	25	100	400	2.05	5.58	
34	1	22.3	25	100	200	2.73	9.4	
35	1	61	25	125	280	1.3	4.06	[3] (2007)
36	1	61	50	100	280	1.3	5.9	
37	1	61	50	125	280	1.3	5.14	
38	1.2	165	50	210	230	2.75	25.25	[66] (2006)
39	1.2	165	50	280	230	2.75	28.4	
40	2.8	207	15	355	230	3.57	61.6	[8] (2009)
41	2.8	207	15	355	230	3.57	65.24	
42	2.8	207	15	355	230	3.57	63.53	
43	2.8	207	15	355	230	3.57	66.52	

Table A1. *Cont.*

No.	tp (mm)	Ep (GPa)	bp (mm)	lb (mm)	bm (mm)	fut (MPa)	Pmax (kN)	Ref. No. (Year)
44	0.17	230	50	200	250	3.35	15.94	[67] (2009)
45	0.17	230	50	200	250	3.35	17.12	
46	0.17	230	50	200	250	3.35	17.66	
47	0.17	230	50	200	250	3.35	19.61	
48	0.17	230	50	200	250	3.35	20.15	
49	0.23	65	50	200	250	3.35	11.69	
50	0.23	65	50	200	250	3.35	13.97	
51	0.23	65	50	200	250	3.35	13.65	
52	0.23	65	50	200	250	3.35	13.2	
53	0.23	65	50	200	250	3.35	14.18	
54	2.8	207	15	336	230	3.57	83.45	[68] (2009)
55	2.8	207	15	336	230	3.57	71.09	
56	2.8	207	15	336	230	3.57	81.48	
57	2.8	207	15	336	230	3.57	70.36	[68] (2009)
58	2.8	207	15	336	230	3.57	59.41	
59	2.8	207	15	336	230	3.57	63.88	
60	2.8	207	15	336	230	3.57	69.41	
61	2.8	207	15	336	230	3.57	84.5	
62	1.2	162	15	241	230	3.55	46.8	[52] (2009)
63	1.2	162	15	328	230	3.55	44	
64	1.2	162	15	328	230	3.55	38.3	
65	1.2	162	15	334	230	3.55	46.7	
66	1.2	162	20	328	230	3.55	50	
67	1.2	162	20	328	230	3.55	51.2	
68	2	65	50	420	230	3.55	22.1	
69	2	65	50	395	230	3.55	21.5	
70	2	65	50	419	230	3.55	21.9	
71	2	65	50	396	230	3.55	18.1	
72	2	65	50	394	230	3.55	24.7	
73	2	65	50	393	230	3.55	24.3	
74	0.62	73	50	386	230	3.55	19.9	
75	0.62	73	50	386	230	3.55	18.6	
76	1.2	162	50	140	230	3.55	26.8	
77	1.2	162	50	210	230	3.55	24.9	
78	1.2	162	50	280	230	3.55	28.4	
79	0.15	80.2	25	150	235	1.57	3.48	[52] (2009)
80	0.15	80.2	25	150	235	1.57	4.81	

Table A1. *Cont.*

No.	tp (mm)	Ep (GPa)	bp (mm)	lb (mm)	bm (mm)	fut (MPa)	Pmax (kN)	Ref. No. (Year)
81	0.15	80.2	25	150	235	1.57	4.69	
82	0.15	80.2	25	150	235	1.57	4.64	
83	0.15	80.2	25	100	235	1.57	3.66	
84	0.15	80.2	25	100	235	1.57	3.17	
85	0.15	80.2	25	100	235	1.57	2.85	
86	0.15	80.2	25	100	235	1.57	3.68	
87	0.15	80.2	25	100	235	1.57	3.79	
88	0.15	80.2	25	200	235	1.57	4.48	
89	0.15	80.2	25	200	235	1.57	5.06	
90	0.15	80.2	25	150	235	1.57	5.27	[9] (2011)
91	0.15	80.2	25	150	235	1.57	4.2	
92	0.15	80.2	25	150	235	1.57	4.89	
93	0.15	80.2	25	150	235	1.57	5.6	
94	0.15	80.2	25	150	235	1.57	4.34	
95	0.15	80.2	25	150	235	1.57	5.49	
96	0.15	80.2	25	150	235	1.57	3.52	
97	0.15	80.2	25	150	235	1.57	4.83	
98	0.15	80.2	25	150	235	1.57	4.53	
99	0.15	80.2	25	150	235	1.57	5.46	
100	0.15	80.2	25	150	235	1.57	4.55	
101	0.15	80.2	25	150	235	1.57	3.73	
102	0.15	80.2	25	150	235	1.57	3.82	
103	0.15	80.2	25	150	235	1.57	4.54	
104	0.15	80.2	25	150	235	1.57	4.06	
105	0.12	216	25	150	235	1.57	4.78	[9] (2011)
106	0.12	216	25	150	235	1.57	4.29	
107	0.12	216	25	150	235	1.57	4.02	
108	0.12	216	25	150	235	1.57	4.33	
109	0.12	216	25	150	235	1.57	4.26	
110	0.13	230	50	150	740	1.0236	5.04	
111	0.13	230	50	150	740	0.80901	3.92	
112	0.13	230	50	150	740	0.780739	4.66	
113	0.13	230	50	150	740	0.897877	4.28	
114	0.13	230	50	150	740	1.077087	4.73	
115	0.13	230	50	150	740	1.107941	4.83	
116	0.13	230	50	150	740	0.991539	3.89	[69] (2009)
117	0.13	230	50	150	740	0.99578	4.01	
118	0.13	230	50	150	740	0.905664	4.2	
119	0.13	230	50	100	740	1.091337	4.93	
120	0.13	230	50	100	740	0.901	4.25	
121	0.13	230	50	100	740	0.981574	4.43	
122	0.13	230	50	100	740	1.03723	4.61	

Table A1. *Cont.*

No.	tp (mm)	Ep (GPa)	bp (mm)	lb (mm)	bm (mm)	fut (MPa)	Pmax (kN)	Ref. No. (Year)
123	0.13	230	50	100	740	0.943638	4.07	[69] (2009)
124	0.13	230	50	100	740	1.002807	3.28	
125	0.13	230	50	100	740	1.012564	4.65	
126	0.13	230	50	100	740	0.96425	3.35	
127	0.13	230	50	50	740	0.921042	2.28	
128	0.13	230	50	50	740	1.048007	2.31	
129	0.13	230	50	50	740	1.353317	4.73	
130	0.13	230	50	50	740	0.914922	2.22	
131	0.13	230	50	50	740	0.954	2.33	
132	0.13	230	50	50	740	0.970059	2.2	
133	0.13	230	50	50	740	1.079692	2.13	
134	0.13	230	50	50	740	0.890021	3.51	

References

1. Kamgar, R.; Bagherinejad, M.H.; Heidarzadeh, H. A new formulation for prediction of the shear capacity of FRP in strengthened reinforced concrete beams. *Soft Comput.* **2020**, *24*, 6871–6887. [CrossRef]
2. Kamgar, R.; Naderpour, H.; Komeleh, H.E.; Jakubczyk–Gałczyńska, A.; Jankowski, R. A proposed soft computing model for ultimate strength estimation of FRP-confined concrete cylinders. *Appl. Sci.* **2020**, *10*, 1769. [CrossRef]
3. Camli, U.S.; Binici, B. Strength of carbon fiber reinforced polymers bonded to concrete and masonry. *Constr. Build. Mater.* **2007**, *21*, 1431–1446. [CrossRef]
4. Chen, J.F.; Teng, J.G. Anchorage strength models for FRP and steel plates bonded to concrete. *J. Struct. Eng.* **2001**, *127*, 784–791. [CrossRef]
5. Tanaka, T. Shear Resisting Mechanism of Reinforced Concrete Beams with CFS as Shear Reinforcement. Bachelors's Thesis, Hokkaido University, Sapporo, Japan, 1996.
6. Maeda, T.; Asano, Y.; Sato, Y.; Ueda, T.; Kakuta, Y. A study on bond mechanism of carbon fiber sheet. Non-Metallic (FRP) Reinforcement for Concrete Structures. In Proceedings of the 3rd International Symposium, Sapporo, Japan, 14–16 October 1997; Japan Concrete Institute: Sapporo, Japan, 1997; Volume 1, pp. 279–285.
7. Kashyap, J.; Willis, C.R.; Griffith, M.C.; Ingham, J.M.; Masia, M.J. Debonding resistance of FRP–to–clay brick masonry joints. *Eng. Struct.* **2012**, *41*, 186–198. [CrossRef]
8. Konthesingha, K.; Masia, M.; Petersen, R.; Page, A. Bond behaviour of NSM FRP strips to modern clay brick masonry prisms under cyclic loading. In Proceedings of the 11th Canadian Masonry Symposium, Toronto, Canada, 31 May–3 June 2009.
9. Oliveira, D.V.; Basilio, I.; Lourenço, P.B. Experimental bond behavior of FRP sheets glued on brick masonry. *J. Compos. Constr.* **2011**, *15*, 32–41. [CrossRef]
10. Mazzuca, P.; Firmo, J.P.; Correia, J.R.; Castilho, E.I. Influence of elevated temperatures on the mechanical properties of glass fibre reinforced polymer laminates produced by vacuum infusion. *Constr. Build. Mater.* **2022**, *345*, 128340. [CrossRef]
11. Carvelli, V.; Pisani, M.A.; Poggi, C. High temperature effects on concrete member reinforced with GFRP rebars. *Compos. Part B Eng.* **2013**, *54*, 125–132. [CrossRef]
12. Rosa, I.C.; Firmo, J.P.; Correia, J.R.; Mazzuca, P. Influence of elevated temperatures on the bond behaviour of sand-coated and ribbed GFRP rebars in concrete—Pull-out tests and calibration of temperature-dependent bond stress vs. slip laws. In *Proceedings of the 10th International Conference on FRP Composites in Civil Engineering, CICE 2021, Istanbul, Turkey, 8–10 December 2021*; Lecture Notes in Civil Engineering Book Series; Springer: Cham, Switzerland, 2022; Volume 198. [CrossRef]
13. Grazzini, A.; Lacidogna, G. Fatigue analysis of FRP strengthened masonry by acoustic emission monitoring. *Key Eng. Mater.* **2019**, *817*, 594–601. [CrossRef]
14. Falborski, T.; Jankowski, R.; Kwiecień, A. Experimental study on polymer mass used to repair damaged structures. *Key Eng. Mater.* **2012**, *488–489*, 347–350. [CrossRef]
15. Falborski, T.; Jankowski, R. Polymeric bearings—A new base isolation system to reduce structural damage during earthquakes. *Key Eng. Mater.* **2013**, *569–570*, 143–150. [CrossRef]
16. Sołtysik, B.; Falborski, T.; Jankowski, R. Preventing of earthquake-induced pounding between steel structures by using polymer elements-experimental study. *Procedia Eng.* **2017**, *199*, 278–283. [CrossRef]
17. Zheng, X.L.; Tao, Y.; Shi, Q.X.; Chen, J.F. Pull-out behaviour of FRP anchors in clay bricks. *Constr. Build. Mater.* **2021**, *283*, 122544. [CrossRef]

18. Zhang, D.; Yang, J.; Chi, L.Y. The bond–slip relationship at FRP–to–brick interfaces under dynamic loading. *Materials* **2021**, *14*, 545. [CrossRef]
19. Mansouri, I.; Hu, J.W.; Kisi, O. Novel predictive model of the debonding strength for masonry members retrofitted with FRP. *Appl. Sci.* **2016**, *6*, 337. [CrossRef]
20. Thamboo, J.; Navaratnam, S.; Poologanathan, K.; Corradi, M. Characteristics of CFRP strengthened masonry wallettes under concentric and eccentric compression. *Case Stud. Constr. Mater.* **2021**, *14*, e00472. [CrossRef]
21. Abdulsalam, B.; Ali, A.H.; ElSafty, A.; Elshafey, N. Behavior of GFRP strengthening masonry walls using glass fiber composite anchors. *Structures* **2021**, *29*, 1352–1361. [CrossRef]
22. Grande, E.; Imbimbo, M.; Sacco, E. Bond behaviour of CFRP laminates glued on clay bricks: Experimental and numerical study. *Compos. Part B Eng.* **2011**, *42*, 330–340. [CrossRef]
23. Kolsch, H. Carbon fiber cement matrix (CFCM) overlay system for masonry strengthening. *J. Compos. Constr.* **1998**, *2*, 105–109. [CrossRef]
24. Galati, N.; Tumialan, G.; Nanni, A. Strengthening with FRP bars of URM walls subject to out–of–plane loads. *Constr. Build. Mater.* **2006**, *20*, 101–110. [CrossRef]
25. Lunn, D.S. Behavior and Modeling of Infill Masonry Walls Strengthened with FRP Using Various End Anchorage. Ph.D. Thesis, North Carolina State University, Raleigh, NC, USA, 2013.
26. Stratford, T.; Pascale, G.; Manfroni, O.; Bonfiglioli, B. Shear strengthening masonry panels with sheet glass–fiber reinforced polymer. *J. Compos. Constr.* **2004**, *8*, 434–443. [CrossRef]
27. Wang, Q.; Chai, Z.; Huang, Y.; Yang, Y.; Zhang, Y. Seismic shear capacity of brick masonry wall reinforced by GFRP. *Asian J. Civ. Eng.* **2006**, *7*, 563–580.
28. Accardi, M.; Cucchiara, C.; La Mendola, L. Bond behavior between CFRP strips and calcarenite stone. In Proceedings of the 6th International Conference on Fracture Mechanics of Concrete and Concrete Structures, Catania, Italy, 17–22 June 2007; pp. 1203–1211.
29. Grande, E.; Milani, G.; Sacco, E. Modelling and analysis of FRP–strengthened masonry panels. *Eng. Struct.* **2008**, *30*, 1842–1860. [CrossRef]
30. Marfia, S.; Sacco, E. Modeling of reinforced masonry elements. *Int. J. Solids Struct.* **2001**, *38*, 4177–4198. [CrossRef]
31. Milani, G.; Rotunno, T.; Sacco, E.; Tralli, A. Failure load of FRP strengthened masonry walls: Experimental results and numerical models. *Struct. Durab. Health Monit.* **2006**, *2*, 29–50. [CrossRef]
32. Yuan, Y.; Milani, G. Closed-form model for curved brittle substrates reinforced with FRP strips. *Compos. Struct.* **2023**, *304*, 116443. [CrossRef]
33. Castellano, A.; Fraddosio, A.; Oliveira, D.V.; Piccioni, M.D.; Ricci, E.; Sacco, E. An effective numerical modelling strategy for FRCM strengthened curved masonry structures. *Eng. Struct.* **2023**, *274*, 115116. [CrossRef]
34. Jing, J.; Zhou, C.; Zhang, C.; Li, T. In-plane cyclic behavior of brick walls strengthened with CFRP plates embedded in the horizontal mortar joint. *J. Build. Eng.* **2023**, *63*, 105476. [CrossRef]
35. Cecchi, A.; Russo, S.; Sciarretta, F. Preliminary investigation on FRP profiles for the structural retrofit of masonry structures. *Key Eng. Mater.* **2017**, *747*, 77–84. [CrossRef]
36. Aiello, M.A.; Sciolti, S. Bond analysis of masonry structures strengthened with CFRP sheets. *Constr. Build. Mater.* **2006**, *20*, 90–100. [CrossRef]
37. Emami, M.; Eftekhar, M.R.; Karimizadeh, H. Experimental study on postponing the deboning of FRP sheets in masonry walls. *Int. J. Archit. Herit.* **2020**, *14*, 314–327. [CrossRef]
38. Mansouri, I.; Kisi, O. Prediction of debonding strength for masonry elements retrofitted with FRP composites using neuro fuzzy and neural network approaches. *Compos. Part B Eng.* **2015**, *70*, 247–255. [CrossRef]
39. Tabari, M.M.R.; Azadani, M.N.; Kamgar, R. Development of operation multi–objective model of dam reservoir under conditions of temperature variation and loading using NSGA–II and DANN models: A case study of Karaj/Amir Kabir dam. *Soft Comput.* **2020**, *24*, 12469–12499. [CrossRef]
40. Abdellahi, M.; Heidari, J.; Bahmanpour, M. A new predictive model for the bond strength of FRP–to–concrete composite joints. *Struct. Concr.* **2014**, *15*, 509–521. [CrossRef]
41. Chen, L.; Kou, C.H.; Ma, S.W. Prediction of slump flow of high–performance concrete via parallel hyper–cubic gene–expression programming. *Eng. Appl. Artif. Intell.* **2014**, *34*, 66–74. [CrossRef]
42. Cevik, A. Modeling strength enhancement of FRP confined concrete cylinders using soft computing. *Expert Syst. Appl.* **2011**, *38*, 5662–5673. [CrossRef]
43. Ebrahimpour, K.H.; Maghsoudi, A. Prediction of curvature ductility factor for FRP strengthened RHSC beams using ANFIS and regression models. *Comput. Concr.* **2015**, *16*, 399–414.
44. Ebrahimpour, K.H.; Maghsoudi, A. Analytical assessment of bending ductility in FRP strengthened RHSC beams. *Civ. Eng. J.* **2018**, *4*, 2719–2737. [CrossRef]
45. Sadeghi, G.; Najafzadeh, M.; Safarzadeh, H. Utilizing gene–expression programming in modelling the thermal performance of evacuated tube solar collectors. *J. Energy Storage* **2020**, *30*, 101546. [CrossRef]
46. Najafzadeh, M.; Niazmardi, S. A novel multiple–kernel support vector regression algorithm for estimation of water quality parameters. *Nat. Resour. Res.* **2021**, *30*, 3761–3775. [CrossRef]

47. Najafzadeh, M.; Homaei, F.; Farhadi, H. Reliability assessment of water quality index based on guidelines of national sanitation foundation in natural streams: Integration of remote sensing and data–driven models. *Artif. Intell. Rev.* **2021**, *54*, 4619–4651. [CrossRef]
48. Kumar, A.; Arora, H.C.; Kumar, K.; Garg, H. Performance prognosis of FRCM-to-concrete bond strength using ANFIS-based fuzzy algorithm. *Expert Syst. Appl.* **2023**, *213*, 119497. [CrossRef]
49. *ACI 440.7R-10*; Guide for the Design and Construction of Externally Bonded Fiber Reinforced Polymer Systems for Strengthening Unreinforced Masonry Structures. ACI Committee: Farmington Hills, MI, USA, 2010.
50. *CNR-DT 200*; Guide for the Design and Construction of Externally Bonded FRP Systems for Strengthening Existing Structures. National Research Council: Rome, Italy, 2013.
51. Ceroni, F.; Ferracuti, B.; Pecce, M.; Savoia, M. Assessment of a bond strength model for FRP reinforcement externally bonded over masonry blocks. *Compos. Part B Eng.* **2014**, *61*, 147–161. [CrossRef]
52. Willis, C.R.; Yang, Q.; Seracino, R.; Griffith, M.C. Bond behaviour of FRP–to–clay brick masonry joints. *Eng. Struct.* **2009**, *31*, 2580–2587. [CrossRef]
53. Carloni, C.; Subramaniam, K.V. FRP/masonry debonding: Numerical and experimental study of the role of mortar Joints. *Compos. Constr.* **2012**, *16*, 581–589. [CrossRef]
54. Khalifa, A.; Gold, W.J.; Nanni, A.; Abdel Aziz, M.I. Contribution of externally bonded FRP to shear capacity of RC flexural members. *J. Compos. Constr.* **1998**, *2*, 195–202. [CrossRef]
55. De Lorenzis, L.; Miller, B.; Antonio, N. Bond of fiber–reinforced polymer laminates to concrete. *Mater. J.* **2001**, *98*, 256–264.
56. Dai, J.; Ueda, T.; Sato, Y. Development of the nonlinear bond stress–slip model of fiber–reinforced plastics sheet–concrete interfaces with a simple method. *J. Compos. Constr.* **2005**, *9*, 52–62. [CrossRef]
57. Sayed–Ahmed, E.; Bakay, R.; Shrive, N. Bond strength of FRP laminates to concrete: State–of–the–art review. *Electron. J. Struct. Eng.* **2009**, *9*, 45–61. [CrossRef]
58. Sato, Y.; Kimura, K.; Kobatake, Y. Bond behaviors between CFRP sheet and concrete. *J. Struct. Constr. Eng.* **1997**, *500*, 75–82. (In Japanese) [CrossRef]
59. Yang, Y.X.; Yue, Q.R.; Hu, Y.C. Experimental study on bond performance between carbon fibre sheets and concrete. *J. Build. Struct.* **2001**, *22*, 36–42. (In Chinese)
60. D'Antino, T.; Pellegrino, C. Bond between FRP composites and concrete: Assessment of design procedures and analytical models. *Compos. Part B Eng.* **2014**, *60*, 440–456. [CrossRef]
61. Neubauer, U.; Rostàsy, F.S. Design aspects of concrete structures strengthened with externally bonded CFRP plates. In Proceedings of the Seventh International Conference on Structural Faults and Repairs, Edinburgh, UK, 8 July 1997; ECS Publications: St. Louis, MO, USA, 1997; pp. 109–118.
62. Van Gemert, D. Force transfer in epoxy-bonded steel–concrete joints. *Int. J. Adhes.* **1980**, *1*, 67–72. [CrossRef]
63. Wu, Y.F.; Jiang, C. Quantification of bond-slip relationship for externally bonded FRP-to-concrete joints. *J. Compos. Constr.* **2013**, *17*, 673–686. [CrossRef]
64. Turco, V.; Galati, N.; De Lorenzis, L.; Modena, C.; Nanni, A. Bond between near–surface mounted FRP rods and masonry in structural strengthening. *Adv. Compos.* **2003**, *4.1*, 209–217.
65. Liu, Y.; Dawe, J.; McInerney, J. Behaviour of GFRP sheets bonded to masonry walls. In Proceedings of the International Symposium on Bond Behaviour of FRP in Structures, Hong Kong, China, 7–9 December 2005; pp. 473–480.
66. Xia, S.; Oehlers, D. Debonding mechanisms in FRP plated unreinforced masonry under out–of–plane loading. *Adv. Struct. Eng.* **2006**, *9*, 619–637. [CrossRef]
67. Lam, C.C. Finite Element Study of Bond-Slip Behaviour of CFRP and GFRP Laminates on brick Masonry. Master's Thesis, Universitat Politècnica de Catalunya, Catalonia, Spain, 2009.
68. Petersen, R.B.; Masia, M.J.; Seracino, R. Bond behavior of near-surface mounted FRP strips bonded to modern clay brick masonry prisms: Influence of strip orientation and compression perpendicular to the strip. *J. Compos. Constr.* **2009**, *13*, 169–178. [CrossRef]
69. La Mendola, L.; Failla, A.; Cucchiara, C.; Accardi, M. Debonding phenomena in CFRP strengthened calcarenite masonry walls and vaults. *Adv. Struct. Eng.* **2009**, *12*, 745–760. [CrossRef]
70. Jakubczyk-Gałczyńska, A.; Jankowski, R. A Proposed Machine Learning Model for Forecasting Impact of Traffic-Induced Vibrations on Buildings. In *Proceedings of the International Conference on Computational Science—ICCS 2020, Amsterdam, The Netherlands, 3–5 June 2020*; Lecture Notes in Computer Science Book Series; Springer: Berlin/Heidelberg, Germany, 2020; Volume 12139, pp. 444–451. [CrossRef]
71. Rojas, R. *Neural Networks: A Systematic Introduction*; Springer: Berlin/Heidelberg, Germany; New York, NY, USA, 1996.
72. Naderpour, H.; Kheyroddin, A.; Amiri, G.G. Prediction of FRP-confined compressive strength of concrete using artificial neural networks. *Compos. Struct.* **2010**, *92*, 2817–2829. [CrossRef]
73. Dehkordi, A.N.; Kamali-Asl, A.; Wen, N.; Mikkelsen, T.; Chetty, I.J.; Bagher-Ebadian, H. DCE-MRI prediction of survival time for patients with glioblastoma multiforme: Using an adaptive neuro-fuzzy-based model and nested model selection technique. *NMR Biomed.* **2017**, *30*, e3739. [CrossRef]
74. Friedman, J.H. Multivariate adaptive regression splines. *Ann. Stat.* **1991**, *19*, 1–67. [CrossRef]
75. Najafzadeh, M.; Oliveto, G. Exploring 3D wave-induced scouring patterns around subsea pipelines with artificial intelligence techniques. *Appl. Sci.* **2021**, *11*, 3792. [CrossRef]

76. Quinlan, J.R. Learning with continuous classes. In Proceedings of the 5th Australian Joint Conference on Artificial Intelligence, Hobart, Tasmania, 16–18 November 1992; pp. 343–348. [CrossRef]
77. Wang, Y.; Witten, I.H. *Induction of Model Trees for Predicting Continuous Classes*; Working Paper 96/23; Department of Computer Science, University of Waikato: Hamilton, New Zealand, 1996.